Optics Letters

Subvolt electro-optical modulator on thin-film lithium niobate and silicon nitride hybrid platform

Abu Naim R. Ahmed,[1,*] **Sean Nelan,**[1] **Shouyuan Shi,**[1] **Peng Yao,**[2] **Andrew Mercante,**[2] **and Dennis W. Prather**[1,2]

[1]*School of Electrical and Computer Engineering, University of Delaware, Newark, Delaware 19716, USA*
[2]*Phase Sensitive Innovations, Newark, Delaware 19711, USA*
Corresponding author: naimece@udel.edu

A low voltage operation electro-optic modulator is critical for applications ranging from optical communications to an analog photonic link. This paper reports a hybrid silicon nitride and lithium niobate electro-optic Mach–Zehnder modulator that employs 3 dB multimode interference couplers for splitting and combining light. The presented amplitude modulator with an interaction region length of 2.4 cm demonstrates a DC half-wave voltage of only 0.875 V, which corresponds to a modulation efficiency per unit length of 2.11 V cm. The power extinction ratio of the fabricated device is approximately 30 dB, and the on-chip optical loss is about 5.4 dB. © 2020 Optical Society of America

https://doi.org/10.1364/OL.381892

An optical modulator is a key building block for photonic integrated circuits (PICs), as its applications are widespread in both analog and digital systems such as on-chip RF photonics [1], passive millimeter wave imaging systems [2], modern telecommunication networks [3,4], data communication [5], frequency comb generation [6], and quantum photonics [7]. The sub-1-volt half-wave voltage (V_π) is a key performance parameter of the optical modulators, as such modulators may be driven without external electrical amplifier circuitry and are compatible with energy efficient ultralow voltage complementary metal–oxide semiconductor (CMOS) electronics [8]. Recently, there has been impressive progress toward ultrawide bandwidth low voltage optical modulators. All silicon (Si)-based [9] optical modulators have been investigated mainly due to standard CMOS fabrication processes that offer excellent scalability. However, free carrier plasma dispersion-based Si modulation limits the extinction ratio and bandwidth. In addition, low second-order nonlinearity, intrinsic absorption loss, undesirable third-order nonlinearities at high optical powers, limited transmission spectrum, and high temperature sensitivity also represent inherent challenges [10,11]. Effort has also been made in silicon–organic hybrid integration to achieve a sub-1-volt modulator [12]; however, the organic nature of these materials raises concerns about long-term stability [13]. For this reason, silicon–organic based devices are not widely considered as an ideal candidate for a scenario that requires

ultrawide bandwidths or environmental stability. In most circumstances, the ideal modulator platform must show a strong electro-optic (Pockels) effect as well as a linear response to the applied voltage. In this context, lithium niobate (LiNbO₃) has been the material of choice due to many interesting physical properties: strong second-order nonlinearity ($\chi^{(2)}$), pure phase modulation without optical absorption, zero to negative chirping, negligible third-order nonlinearity, better temperature stability, and a wide transmission spectrum [3,14,15]. However, conventional bulk LiNbO₃ modulators suffer from large optical mode size with weak confinement, and large bending radii due to their low index contrast (< 0.02). This necessitates for metal electrodes to be placed farther from the optical waveguide, to avoid metal related absorption loss, and thus significantly increase the half-wave voltage. For example, a typical long bulk LiNbO₃ Mach–Zehnder modulator (MZM) demonstrates a V_π of 3–8 V [3,16]. To address this limitation, recent advances in crystalized ion sliced (CIS) thin-film LiNbO₃ on insulator (TFLNOI) devices have shown great promise in overcoming these drawbacks of bulk LiNbO₃. To this end, TFLNOI offers almost a 20 times smaller optical mode size with tighter mode confinement compared to bulk LiNbO₃. Consequently, TFLNOI modulator metal electrodes can be placed closer to the optical waveguide, thereby resulting in enhanced modulation efficiency and lower power consumption for switching applications, and they facilitate PIC integrable devices. Low loss, ultrawide bandwidth, and low voltage modulators have been demonstrated in pure TFLNOI platforms [10,11,17–20]. The lowest V_π of 1.4 V for a 2 cm device length was demonstrated in TFLNOI [19]. In other works, the hybrid integration of LiNbO₃ with different materials (e.g., Si, SiN$_x$, Ta₂O₅, ChG) has been pursued to avoid the direct etching of LiNbO₃ [20–28]. Silicon nitride (SiN$_x$) is the ideal material among all of these due to its intrinsic material properties: similar refractive index to LiNbO₃, ultralow propagation loss, low second-order nonlinearity, a small thermo-optic coefficient, very high-power handling capability, and PIC compatibility [29,30]. The lowest V_π reported in this hybrid LiNbO₃ − SiN$_x$ platform was 2.5 V for a 1.2-cm-long device [23]. A sub-1-volt V_π modulator in both standalone and hybrid thin-film LiNbO₃ has not yet been demonstrated.
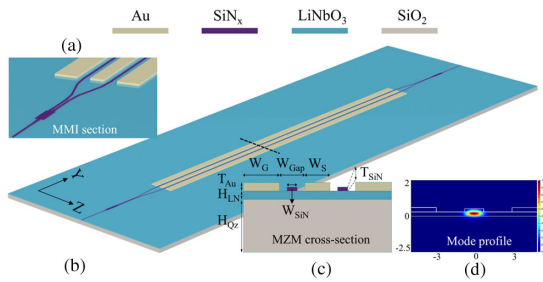
Fig. 1. (a) Schematics of the 1×2 MMI splitter section of the sub-1-volt MZ modulator section. (b) 3D schematic view of the complete thin-film modulator layout with hybrid $LiNbO_3 - SiNx$ MZM and electrodes. The dimensions are not to scale. (c) Cross section of the MZM in the lateral $x - z$ plane, with different fabrication parameters called out. (d) Simulated TE optical mode profile at one arm of the modulator, where the lateral mode is guided by a 220 nm $\times$ 1.5 μm SiN_x loading strip, and optical wavelength is 1550 nm.

In this work, a subvolt hybrid $LiNbO_3 - SiN_x$ electro-optic MZM with a push–pull scheme is demonstrated, where the MZM is realized using a multimode interferometric (MMI) splitter and combiner [Fig. 1(a)]. The subvolt V_π value of the present device is achieved by simply increasing the device length and reducing the electrode gap while maintaining the high electrical and optical field overlap at the $LiNbO_3$ region. To the best of our knowledge, this is the first time an MMI has been designed, simulated and characterized for realizing the MZM in this hybrid $LiNbO_3$ platform. The fabricated device achieved a measured V_π of 0.875 V with a 2.4 cm long interaction region. A high-power extinction ratio of approximately 30 dB is also measured. This subvolt MZM can be driven without external voltage driving circuitry, which significantly improves the cost of implementation and overall power consumption [31]. This paper is organized by first presenting the design and simulation of the optical waveguide and the 1×2 MMI splitter. Then device fabrication is discussed briefly, followed by the optical and DC characterization of the MZM.

The 3D schematic structure of the subvolt electro-optic modulator, in the hybrid $SiNx - LiNbO_3$ platform, is shown in Fig. 1(b). The cross-section of the modulator is shown in Fig. 1(c), which consists of approximately 220 nm plasma-enhanced chemical vapor deposition (PECVD) SiN_x strip on top of the 300 nm X-cut thin-film $LiNbO_3$ (H_{LN}) overlaid with a 4 μm SiO_2 bottom cladding layer. To laterally confine the fundamental transverse electric (TE) mode, the width (W_{SiN}) and thickness (T_{SIN}) of the strip loaded waveguide are chosen as 1.5 μm and 0.22 μm, respectively. The chosen dimension also offers a simulated bending loss of less than 0.01 dB/90° bend for 300 μm radii. The TE optical mode profile at one of the modulator arms is depicted in Fig. 1(d), where the mode confinement factor in the $LiNbO_3$ is approximately 65% for this configuration. The subvolt modulator is implemented using a push-pull MZM configuration. Here, the optical signal is equally split into two paths, and each arm is modulated by opposite electric fields, directed by applying a voltage on the push-pull configured electrodes. This configuration requires a $\pi/2$-phase shift in each arm to produce a total π-phase shift which reduces the voltage requirement by a factor of two for a π-phase shift. An MMI splitter and combiner are used as a 3 dB coupler for MZM configurations. Unlike directional couplers and Y-splitters, which are very sensitive to the waveguide dimension and, therefore, require precise lithography, the

MMI coupler offers large fabrication tolerances as well as large bandwidth and polarization insensitivity [32]. A 1×2 MMI is used as a 3 dB splitter from the input section, which is connected to an optical bend with a bend radius of 500 μm. Then, respective 2.4 cm modulator arms are connected to the bend sections. Following modulation, the two arms are combined using a 2×1 MMI. The 1×2 MMI couplers operate based on the self-imaging principle [32,33], where reconstruction of the original input field happens after defined propagation distances. Therefore, the length of the MMI region (L_{MMI}) requires careful design to accurately reconstruct the input port field to the two-output port fields. The width of the MMI (W_{MMI}) is set to 7.2 μm to avoid evanescent coupling between the two output modes, which yields a separation distance of 4 μm between the two modes. The initial length of the multimode region is estimated using the self-imaging property of multimode waveguides. The length of the MMI region based on the 2D approximation is given by $L_{MMI} = \frac{3\pi}{8(\beta_0 - \beta_1)}$. Here, β_0 and β_1 are defined as the propagation constant of the two lowest order TE modes, where $\beta = n_{eff} \frac{2\pi}{\lambda}$. The effective indices for the two lowest order modes are found to be 1.91 and 1.90, and β_0 and β_1 are calculated to be 7.76 and 7.72, respectively. This results in a length of 36.79 μm. For further optimization of the design parameters, Lumerical's MODE simulation software is used. With an MMI section width of $W_{MMI} = 7.2$ μm, length of $L_{MMI} = \sim 36.8$ μm, and separation between output waveguide of $S_{MMI} = 4$ μm, the final dimensions of the structure are optimized by sweeping the MMI length for fixed W_{MMI} and S_{MMI}, as shown in Fig. 2(a). According to the simulation results, maximum transmission occurs at an MMI length of $\sim$38 μm, which is very close to the length given by the self-imaging method. For further reduction of the mode mismatch between the MMI region and the input waveguide, linear tapers are introduced at the input and output section. The required taper length (L_{taper}) and input/output taper width (W_{taper}) are obtained by performing a length and width sweep in Lumerical's MODE solver. From Fig. 2(b), it is shown that 80 μm is a sufficient length for maximum transmission. Therefore, the optimized design parameters are $W_{MMI} = 7.2$ μm, $S_{MMI} = 4$ μm, $L_{MMI} = \sim 38$ μm, $W_{taper} = 3$ μm, and $L_{taper} = 80$ μm. An electric field profile for the designed two-fold self-image MMI is shown in Fig. 2(c). A highly confined optical mode together with closely placed electrodes in TFLNOI significantly reduces the V_π of the optical modulator. Here, the optical waveguides are propagated in the y-crystal direction, and the integrated electrodes are placed such that the maximum r_{33} coefficient is achieved for the TE optical mode. This will also confirm the strong modal overlap between the electrical signal and the fundamental TE optical mode. A ground–signal–ground (GSG) electrode configuration is used to realize the desired push–pull modulation, the gap between the electrodes (W_{Gap}) is 6 μm to maintain an acceptable metal absorption loss. The simulated metal absorption loss for a waveguide centered within electrodes possessing a 6 μm gap is 0.12 dB/cm. The calculated electric field strength in the waveguide region is 1.5×10^5 V/m for a 1 V applied voltage. The strong electric field strength in the EO material yields efficient EO modulation. Given the simulated guided optical field and electrode gap, the calculated V_π is 0.86 V for a 2.4-cm-long device at 1550 nm wavelength [23].

A 300 nm X-cut TFLNOI is used as a substrate, which is procured from NanoLN. A 220 nm thin film of SiN_x is deposited on top of the thin-film $LiNbO_3$ using PECVD. The measured refractive index is 1.943 at 1550 nm for the SiN_x layer. The
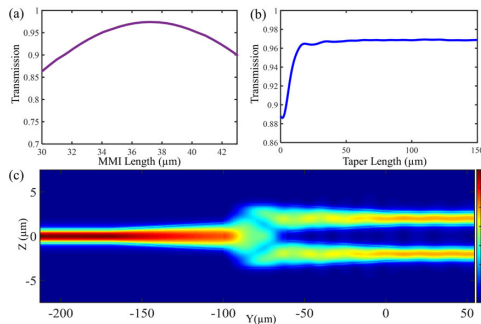
Fig. 2. (a) Simulated transmitted power for different MMI lengths (L_{MMI}). (b) Simulated transmitted power for different taper lengths (L_{taper}). (c) Electric field distribution in a 1×2 MMI in the $zn - y$ plane. Here, LMMI = ~ 38 μm, $W_{MMI} = 7.2$ μm, $W_{taper} = 3$ μm, and $L_{taper} = 80$ μm. The above result is obtained using the Lumerical MODE solver.

optical waveguides and MZM are defined on the SiN_x layer by electron-beam lithography using a similar process described in a previous work [30]. The electrodes are defined using the laser writer (Heidelberg MLA 100), which maintains precise alignment to avoid excessive metal absorption loss. A bilayer lift-off process is used to pattern a 300-nm-thick metal electrode. Finally, the device's waveguide facets are diced and polished for efficient fiber-chip coupling. The complete fabrications steps are illustrated in Fig. 3(a). The scanning electron micrograph (SEM) images and microscopic image of the fabricated modulator with the integrated electrode are shown in Figs. 3(b)–3(e). The experimental setup is shown in Fig. 3(f). The fabricated device electrode gap is reduced to 5.8 μm from the designed value of 6 μm, and the waveguide is closer to the signal electrode due to the fabrication tolerances.

To characterize the 3 dB MMI splitter, 1550 nm light from a tunable telecom laser (Keysight 81608A) is launched into the device using a 2 μm spot size polarization maintenance lensed fiber. The near-field output image of the 1×2 MMI splitter end facets is captured by an infrared camera (Inficon) using a high numerical aperture lens. The near field image for the standard 1×2 splitter is shown in Fig. 4(a) inset. The output image
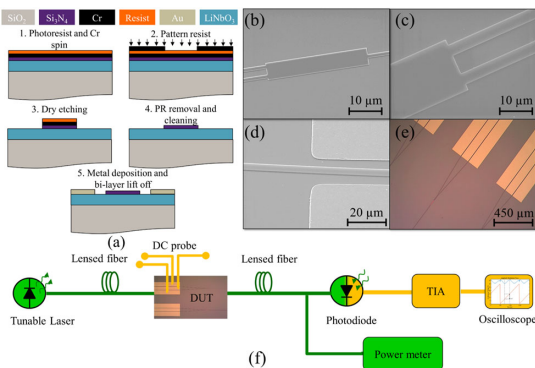

Fig. 3. (a) Schematic of the fabrication flow of the hybrid $Si_3N_4 - LiNbO_3$ based racetrack device. (b) SEM image of the fabricated 1×2 MMI. (c) Close-up SEM image of the fabricated 1×2 MMI output section. (d) Close-up SEM image of the metal electrode and optical waveguide. (e) Microscopic image of the fabricated MZM. (f) Experimental setup for the DC characterization of the subvolt modulator. The green line indicates the optical domain, and the yellow line indicates the electrical domain.
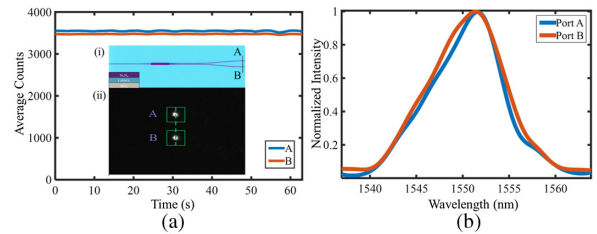

Fig. 4. (a) Average pixel count in the A and B region [inset (ii)] of the output MMI port recorded using image processing software. Inset (i) shows the top schematic view of the 1×2 MMI and corresponding output arm, and inset (ii) is the infrared camera image showing the light emerging from the 1×2 MMI output section. (b) Measured normalized transmission versus wavelength for port A and B.

and pixel counts are extracted using image processing software. The total average intensity counts of the MMI arm A and B are extracted by drawing a box as shown in the Fig. 4(a) inset. The average box count for A and B over 60 s is shown in Fig. 4(a). The measured splitting ratio is 48.6:51.4 for the designed MMI. The power imbalance, defined as the ratio of output power in dB, is 0.57 dB at 1550 nm. The transmission spectra from the input to the two output ports of the MMI coupler are extracted using a tunable laser source by sweeping 1535 to 1565 nm. The normalized output spectra from both output ports is almost identical, as shown in Fig. 4(b). The bandwidth of the MMI is wavelength-dependent as the 3 dB coupling length depends on λ^{-1} [33]. The imbalance may occur due to deviation from the design dimensions from the fabrication and fiber alignment tolerances. The MZM device is characterized by measuring the voltage required to induce a π-phase difference between the two modulator arms. The tunable laser source is coupled to the device under test (DUT) using a lensed fiber, which is aligned to launch TE-polarized light at 1550 nm. The output light is detected by an InGaAs photodetector (DET01CFC) through another TE-polarized lensed fiber and directed to an oscilloscope via a trans-impedance amplifier (TIA). The total optical insertion loss from the input fiber to the output fibers is measured to be ~ 19 dB, largely due to coupling losses at the end facets. The on-chip optical loss of 5.4 dB and coupling loss of ~ 6.8 dB/facet are measured for this type of the device via the cutback method. For the ~ 5.8 μm electrode, the metal-induced absorption loss is below 0.2 dB/cm. By introducing a mode matching inverse taper and leveraging high-quality low pressure chemical vapor deposition (LPCVD) SiN_x rather than PECVD SiN_x, the total insertion loss can be significantly reduced. The MZM's electrodes are driven in a push–pull configuration, so that phase is delayed on one arm and advanced on the other arm. A low-speed triangular voltage sweep is applied to the modulator electrode via a DC needle probe. Voltage measurements for both push–pull and single arm configurations are performed. The measured half-wave voltage (V_π) for the push–pull configuration is 0.875 V [Fig. 5(a)], while for the single arm the V_π is 1.58 V [Fig. 5(b)]. This indicates that push–pull configuration V_π is roughly half of the single arm V_π. The discrepancy could be resulting from the fringing field effect due to floating ground in the single arm V_π measurement, and further investigation is needed to confirm this variation. The corresponding voltage-length product for this 2.4 cm push-pull MZM is 2.11 V cm. This modulation efficiency is improved by a factor of 5, compared to the bulk $LiNbO_3$ counterpart [34], and comparable to the lowest achievable nonhybrid TFLNOI modulator [19]. The
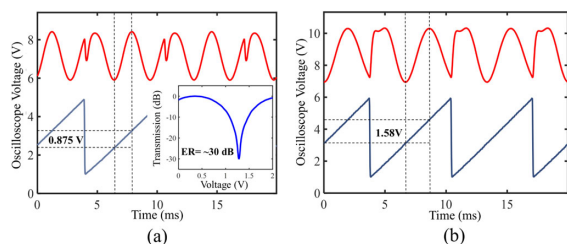
Fig. 5. (a) Measured data from the DC V_π measurement and the applied electrical signal (blue), as well as the resultant amplitude modulated signal traces (red), are shown. The measured V_π is 0.875 V and V_π L of 2.11 V cm. The inset shows the measured extinction ratio in dB. (b) DC V_π measurement of a single-arm-driven MZM where the second arm is ungrounded. The measured V_π is 1.58 V, which is nearly double of the push–pull configuration.

measured V_π is slightly higher than our calculated value, which may be due to the discrepancy between simulated and actual mode confinement factor and group index. The demonstrated subvolt V_π modulator would be drivable from direct CMOS circuitry. Importantly, this subvolt modulator also exhibits a high extinction ratio of approximately 30 dB, which is shown by plotting the normalized optical transmission in logarithmic scale as in Fig. 5(a) inset. The proposed hybrid device is functional up to several GHz according to sideband measurements for the similar length phase modulator. The high-speed modulation of the proposed device can be achieved by careful design of the traveling wave electrode (electrode gap, height, signal width), for impedance matching and group index matching, which is currently ongoing and will be reported in later work.

In summary, an electro-optic MZM modulator with a sub-1-volt halfwave voltage has been demonstrated. To the best of our knowledge, this is the lowest halfwave voltage (V_π) shown for any thin-film lithium-niobate-based electro-optic modulator. The modulator features a V_π of 0.875 V and a power extinction ratio of 30 dB. In addition, a compact 38-μm-long hybrid 3 dB MMI splitter has been designed, simulated, fabricated, and characterized. The measured power imbalance between the two MMI output arms is about 0.5 dB at 1550 nm. We believe that this work provides a pathway towards future sub-1-V driven high bandwidth electro-optic modulators by careful design and optimization of the traveling wave electrodes.

Disclosures. The authors declare no conflicts of interest.

REFERENCES

1. R. C. Williamson and R. D. Esman, J. Lightwave Technol. **26**, 1145 (2008).
2. C. A. Schuetz, J. Murakowski, G. J. Schneider, and D. W. Prather, IEEE Trans. Microwave Theory Tech. **53**, 1732 (2005).
3. E. L. Wooten, K. M. Kissa, A. Yi-Yan, E. J. Murphy, D. A. Lafaw, P. F. Hallemeier, D. Maack, D. V. Attanasio, D. J. Fritz, G. J. McBrien, and D. E. Bossi, IEEE J. Sel. Top. Quantum Electron. **6**, 69 (2000).
4. D. A. Miller, J. Lightwave Technol. **35**, 346 (2017).
5. Q. Cheng, M. Bahadori, M. Glick, S. Rumley, and K. Bergman, Optica **5**, 1354 (2018).
6. C. Wang, M. Zhang, R. Zhu, H. Hu, and M. Loncar, "Monolithic photonic circuits for Kerr frequency comb generation, filtering and modulation," arXiv: 1809.08637 (2018).
7. K. F. Reim, J. Nunn, V. O. Lorenz, B. J. Sussman, K. C. Lee, N. K. Langford, D. Jaksch, and I. A. Walmsley, Nat. Photonics **4**, 218 (2010).
8. Y. Shi, C. Zhang, H. Zhang, J. H. Bechtel, L. R. Dalton, B. H. Robinson, and W. H. Steier, Science **288**, 119 (2000).
9. G. T. Reed, G. Mashanovich, F. Y. Gardes, and D. J. Thomson, Nat. Photonics **4**, 518 (2010).
10. C. Wang, M. Zhang, B. Stern, M. Lipson, and M. Lončar, Opt. Express **26**, 1547 (2018).
11. A. Rao and S. Fathpour, IEEE J. Sel. Top. Quantum Electron. **24**, 3400114 (2018).
12. R. Ding, T. Baehr-Jones, W.-J. Kim, A. Spott, M. Fournier, J.-M. Fedeli, S. Huang, J. Luo, A. K.-Y. Jen, L. Dalton, and M. Hochberg, J. Lightwave Technol. **29**, 1112 (2011).
13. M.-C. Oh, H. Zhang, C. Zhang, H. Erlig, Y. Chang, B. Tsap, D. Chang, A. Szep, W. H. Steier, H. R. Fetterman, and L. R. Dalton, IEEE J. Sel. Top. Quantum Electron. **7**, 826 (2001).
14. D. Janner, D. Tulli, M. García-Granda, M. Belmonte, and V. Pruneri, Laser Photon. Rev. **3**, 301 (2009).
15. L. Arizmendi, Phys. Status Solidi A **201**, 253 (2004).
16. J. Macario, P. Yao, S. Shi, A. Zablocki, C. Harrity, R. D. Martin, C. A. Schuetz, and D. W. Prather, Opt. Express **20**, 23623 (2012).
17. A. J. Mercante, S. Shi, P. Yao, L. Xie, R. M. Weikle, and D. W. Prather, Opt. Express **26**, 14810 (2018).
18. T. Ren, M. Zhang, C. Wang, L. Shao, C. Reimer, Y. Zhang, O. King, R. Esman, T. Cullen, and M. Lončar, IEEE Photon. Technol. Lett. **31**, 889 (2019).
19. C. Wang, M. Zhang, X. Chen, M. Bertrand, A. Shams-Ansari, S. Chandrasekhar, P. Winzer, and M. Lončar, Nature **562**, 101 (2018).
20. A. Honardoost, F. A. Juneghani, R. Safian, and S. Fathpour, Opt. Express **27**, 6495 (2019).
21. M. He, M. Xu, Y. Ren, J. Jian, Z. Ruan, Y. Xu, S. Gao, S. Sun, X. Wen, L. Zhou, L. Liu, C. Guo, H. Chen, S. Yu, L. Liu, and X. Cai, Nat. Photonics **13**, 359 (2019).
22. X. Weigel, J. Zhao, K. Fang, H. Al-Rubaye, D. Trotter, D. Hood, J. Mudrick, C. Dallo, A. T. Pomerene, A. L. Starbuck, C. T. DeRose, A. L. Lentine, G. Rebeiz, and S. Mookherjea, Opt. Express **26**, 23728 (2018).
23. S. Jin, L. Xu, H. Zhang, and Y. Li, IEEE Photon. Technol. Lett. **28**, 736 (2016).
24. A. Rao, A. Patil, P. Rabiei, A. Honardoost, R. DeSalvo, A. Paolella, and S. Fathpour, Opt. Lett. **41**, 5700 (2016).
25. P. Rabiei, J. Ma, S. Khan, J. Chiles, and S. Fathpour, Opt. Express **21**, 25573 (2013).
26. A. Rao, A. Patil, J. Chiles, M. Malinowski, S. Novak, K. Richardson, P. Rabiei, and S. Fathpour, Opt. Express **23**, 22746 (2015).
27. A. N. R. Ahmed, S. Shi, M. Zablocki, P. Yao, and D. W. Prather, Opt. Lett. **44**, 618 (2019).
28. A. N. R. Ahmed, A. Mercante, S. Shi, P. Yao, and D. W. Prather, Opt. Lett. **43**, 4140 (2018).
29. R. Baets, A. Z. Subramanian, S. Clemmen, B. Kuyken, P. Bienstman, N. Le Thomas, G. Roelkens, D. Van Thourhout, P. Helin, and S. Severi, in *Optical Fiber Communications Conference and Exhibition (OFC)* (IEEE, 2016), pp. 1–3.
30. A. N. R. Ahmed, S. Shi, A. J. Mercante, and D. W. Prather, Opt. Express **27**, 30741 (2019).
31. S. Wolf, M. Lauermann, P. Schindler, G. Ronniger, K. Geistert, R. Palmer, S. Köber, W. Bogaerts, J. Leuthold, W. Freude, and C. Koos, J. Lightwave Technol. **33**, 1425 (2015).
32. J. Leuthold and C. H. Joyner, J. Lightwave Technol. **19**, 700 (2001).
33. A. Maese-Novo, R. Halir, S. Romero-García, D. Pérez-Galacho, L. Zavargo-Peche, A. Ortega-Moñux, I. Molina-Fernández, J. G. Wangüemert-Pérez, and P. Cheben, Opt. Express **21**, 7033 (2013).
34. Thorlabs—LN81S-FC 10 GHz intensity modulator, X-Cut, FC/PC connectors, https://www.thorlabschina.cn/thorproduct.cfm?partnumber=LN81S-FC.